Global Elastic Response Simulation

Project Representative
Seiji Tsuboi — Institute for Research on Earth Evolution / Data Research Center for Marine-Earth Sciences, Japan Agency for Marine-Earth Science and Technology

Authors
Seiji Tsuboi — Institute for Research on Earth Evolution / Data Research Center for Marine-Earth Sciences, Japan Agency for Marine-Earth Science and Technology
Nozomu Takeuchi — Earthquake Research Institute, The University of Tokyo

In this project, we conduct waveform inversion to obtain detailed whole mantle seismic velocity model using the direct solution method. Here we compare our new model with previous model and discuss which features are newly identified in our new model. We also pursue accurate numerical techniques to obtain theoretical seismic waves for realistic three dimensional (3-D) Earth models using Spectral-Element Method. We calculate synthetic seismic waveform for 2011 Tohoku earthquake (Mw9.0) using fully 3-D Earth model. Our results indicate that the earthquake rupture model we have used for this simulation is fairly accurate to grasp the rupture propagation along the earthquake fault.

Keywords: Synthetic seismograms, 3-D velocity structure of the Earth, Spectral Element Method

1. Comparison of SH18CEX and SH18CE

We previously obtained the whole mantle SH velocity models, SH18CE (Takeuchi, 2007 [1]; Tsuboi and Takeuchi, 2007 [2]) and SH18CEX (Tsuboi and Takeuchi, 2011 [3]). In this paper, we compare these two models and discuss which features are newly identified in SH18CEX. We also discuss which part of the dataset contributed to the improvements.

The data set used in obtaining SH18CEX is a combination of the data set of SH18CE (hereafter, referred to as "Data Set 1") and the new data set (hereafter, referred to as "Data Set 2"). Data Set 1 includes only data for large events (Mw ≧ 6.5), whereas Data Set 2 includes data for smaller events (the smallest *Mw* is 6.0). The entire data set used for SH18CEX consists of 54,790 traces (271,798 time windows), which is approximately 3.5 times the number of traces used for SH18CE. With the exception of the data set used, the methods and parameters employed are exactly the same.

First, we compare the lowermost mantle models of SH18CEX and SH18CE via visual inspection (Fig. 1). We see that the overall patterns, i.e., the long-wavelength features,

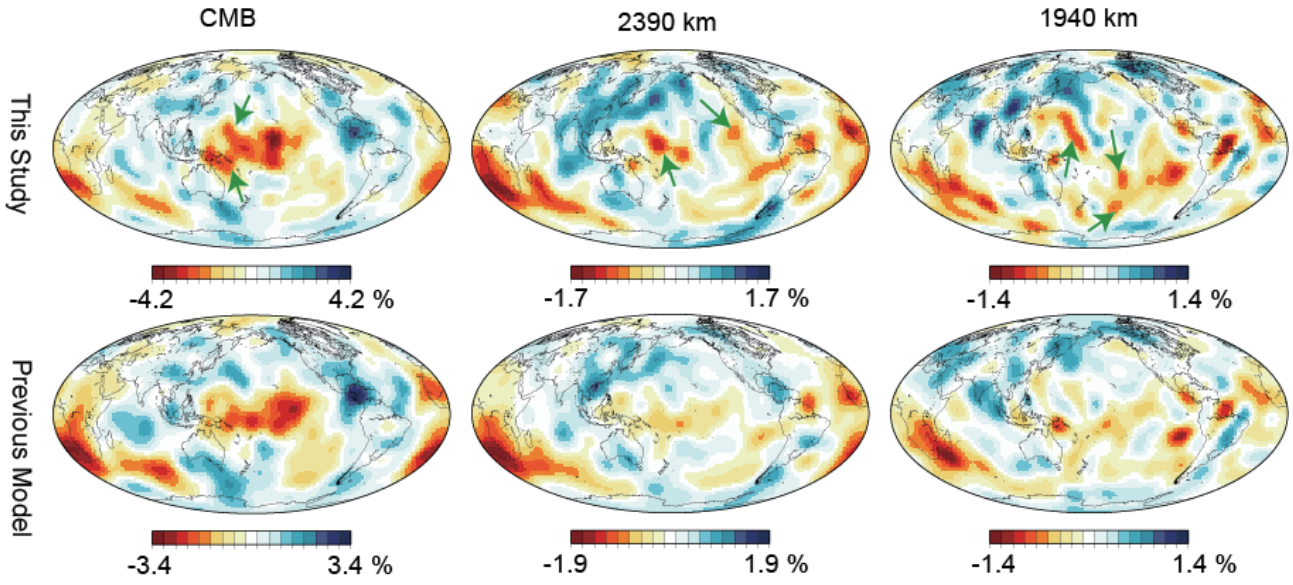

Fig. 1 Comparison between SH18CEX (upper figures) and SH18CE (lower figures) in the lowermost mantle. The green arrows indicate examples of the prominent features observed only in SH18CEX.

Table 1 Comparison of variance improvements.

	Data Set 1		Data Set 2	
	SH18CE	SH18CEX	SH18CE	SH18CEX
200-400 s	42 %	44 %	30 %	32 %
100-200 s	41 %	42 %	33 %	37 %
50-100 s	34 %	31 %	23 %	31 %

	Data Set 2 (Mw ≥ 6.5)		Data Set 2 (Mw < 6.5)	
	SH18CE	SH18CEX	SH18CE	SH18CEX
200-400 s	36 %	38 %	20 %	21 %
100-200 s	34 %	38 %	32 %	36 %
50-100 s	21 %	30 %	24 %	32 %

of the two models are nearly invariant, but the significant differences between the models are the relatively small-scale anomalies observed only in SH18CEX (such as the features indicated by the green arrows in Fig. 1). This can probably be attributed to the resolution improvement in the new model.

The newly identified small-scale features appear to be constrained primarily by the body waveforms in Data Set 2. Table 1 summarizes the variance improvements due to SH18CE and SH18CEX. SH18CEX exhibits improvements comparable with those of SH18CE for the periodic ranges of 200-400 s and 100-200 s (Table 1, top). For the periodic range of 50-100 s, SH18CEX also exhibits comparable improvements for the existing data (34% for SH18CE and 31% for SH18CEX); on the other hand, it exhibits greater improvements for the incremental data (23% for SH18CE and 31% for SH18CEX) (Table 1, top). Improvements for the incremental data themselves are not surprising because they are included only in the inversion for SH18CEX, but note the larger improvements for the periodic range of 50-100 s compared with the other ranges. Considering that the data set of 50-100 s primarily consists of body waveforms, the results suggest that the incremental constraints on the Earth's structures are primarily attributable to the body waveforms in the incremental data set.

For the periodic range of 200-400 s, the improvements for Data set 1 are greater than those for Data set 2 (e.g., 44% and 32%, respectively, for SH18CEX) (Table 1, top). This is probably due to the fact that the signal-to-noise ratios of Data Set 2 are not adequate for longer periods because Data Set 2 includes data for smaller events. Indeed, for the periodic range of 200-400 s, variance improvements for larger events (Mw ≧ 6.5) are significantly larger than those for the data for smaller events (Mw < 6.5) (38 % and 21 %, respectively, for SH18CEX) (Table 1, bottom). However, note that this does not hold for the periodic range of 50-100 s (30% and 32%, respectively, for SH18CEX) (Table 1, bottom), which suggests that such problems are not encountered in this periodic range. Therefore, we can conclude that the small-scale features in the lower mantle would be better constrained by the incremental data set.

2. 2011 Tohoku earthquake

2.1 Earthquake rupture mechanism

We apply the waveform inversion to obtain slip distribution in the source fault at the 2011 Tohoku earthquake in the same manner as our previous work (Nakamura et al., 2010 [4]). We use 22 broadband seismograms of IRIS GSN seismic stations with epicentral distance between 30 and 100 degrees. The broadband original data are integrated into ground displacement and band-pass filtered in the frequency band 0.002-1 Hz. We use the velocity structure model IASP91 (Kennet and Engdahl, 1991 [5]) to calculate the wavefield near source and stations. We assume that the strike of the fault plane is 201 degree and the dip angle is 9 degree, based on Global Centroid Moment Tensor solution. The length of subfault used for our inversion is 30 km in the strike direction and 20 km in the dip direction. The assumed fault length is totally 460 km consistent with the aftershock distribution. We assume that rupture velocity along the fault is about 2.0 km/s. The results of the inversion show the bilateral rupture to the northeast and southwest with two main asperities along the fault; the maximum slip of 49 m with the reverse fault mechanism at approximately 100 km northeast of the epicenter and another large slip with reverse fault mechanism at 100 km southwest of the epicenter. The total amount of the released seismic moment corresponds to moment magnitude Mw=9.1. The duration of source time function is 150 sec. The fault length of 450 km and the source duration time of 150 sec are typical for Mw 9.1 earthquake. However, the maximum slip of 49 m is unusually large. Also the rupture velocity of 2.0 km/s may characterize this earthquake as slow tsunami generating earthquake. We should note that the fault rupture model, we have obtained, is not unique in the sense that the variance reduction is not significant. There are possibilities of other models, which show much slower rupture velocity or larger slip. Thus, we examine the validity of these fault rupture parameters by comparing the theoretical seismograms computed for this fault model with the observed seismograms.

2.2 Broadband synthetic seismograms

We calculate broadband synthetic seismograms with this source propagation model for a realistic 3D Earth model using the spectral-element method (Komatitsch and Tromp, 2002 [6]). The simulations are performed using 726 processors, which require 91 nodes of the Earth Simulator 2. We use a mesh with 200 million spectral-elements, for a total of 13 billion global integration grid points. This translates into an approximate grid spacing of 2.0 km along the Earth's surface. On this number of nodes, a simulation of 30 minutes of wave propagation accurate at periods of 3.5 seconds and longer requires about 7 hours of CPU time. An example of waveform matches are shown in Fig. 2, where three component broadband seismograms are compared with the observations at teleseismic stations, AFI

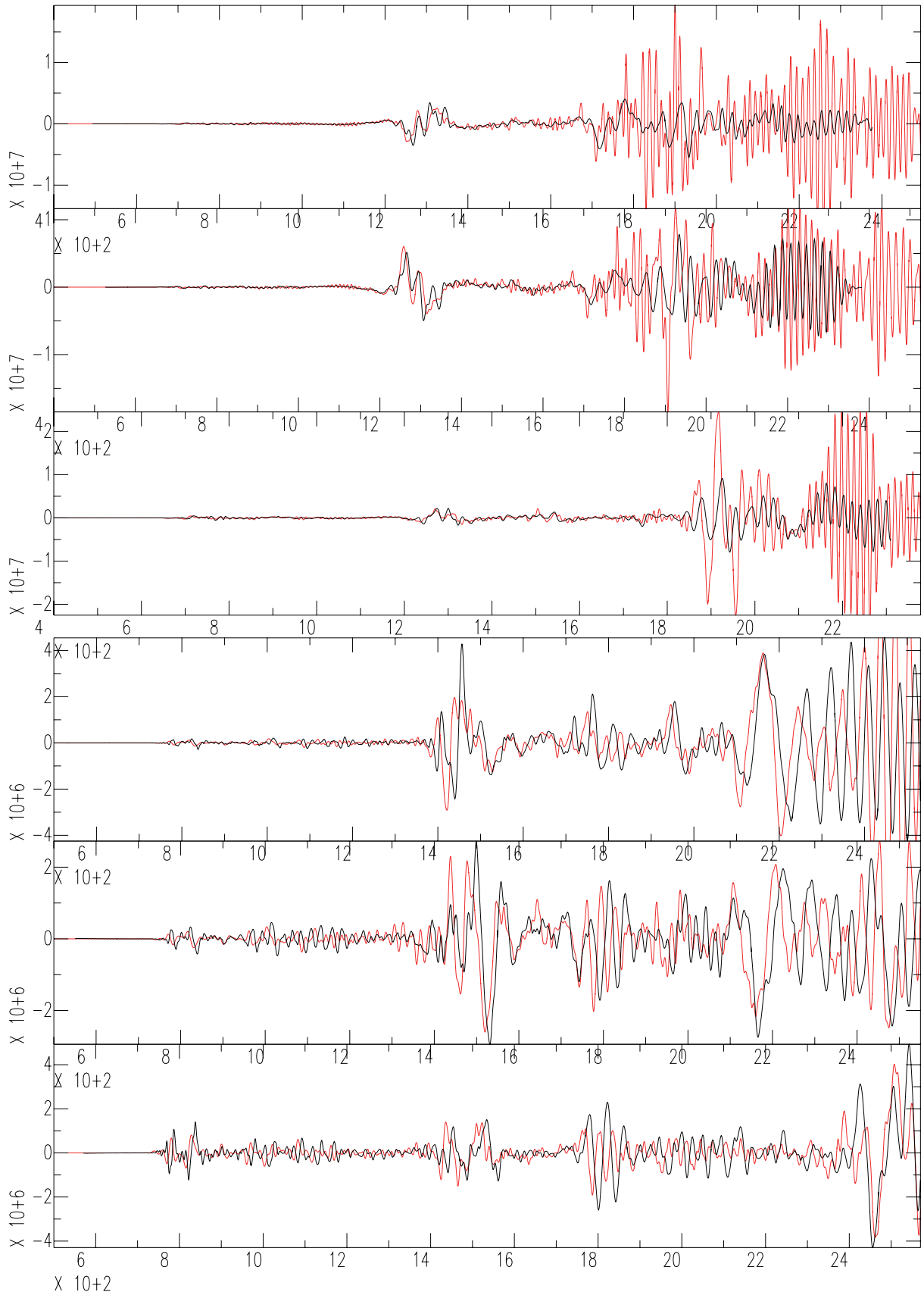

Fig. 2 Comparisons of synthetic seismograms and observation for IRIS GSN station AFI (top), ESK (bottom), where the epicentral distances are 67 degree, 81 degree, respectively. The synthetics and the observations are in red and black, respectively. Instrument responses are convolved to synthetics to convert them to ground velocity. Traces are EW, NS, and UD components from top to bottom, respectively. The origin of the time axis is origin time of the event and the vertical axis shows digital count. All of the traces are bandpass filtered between 500 sec and 10 sec.

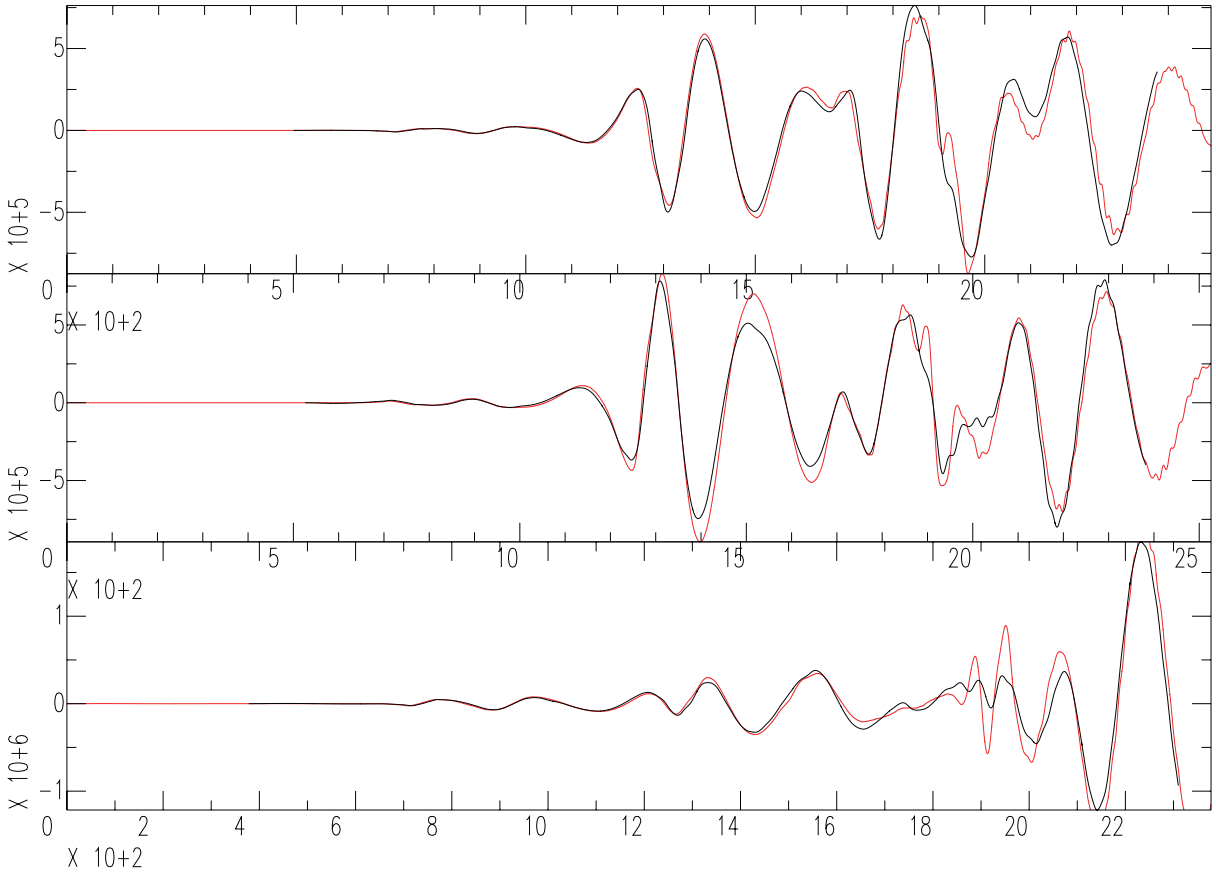

Fig. 3 Comparisons of synthetic seismograms for station AFI. Bandpass filtered at 500 sec and 200 sec.

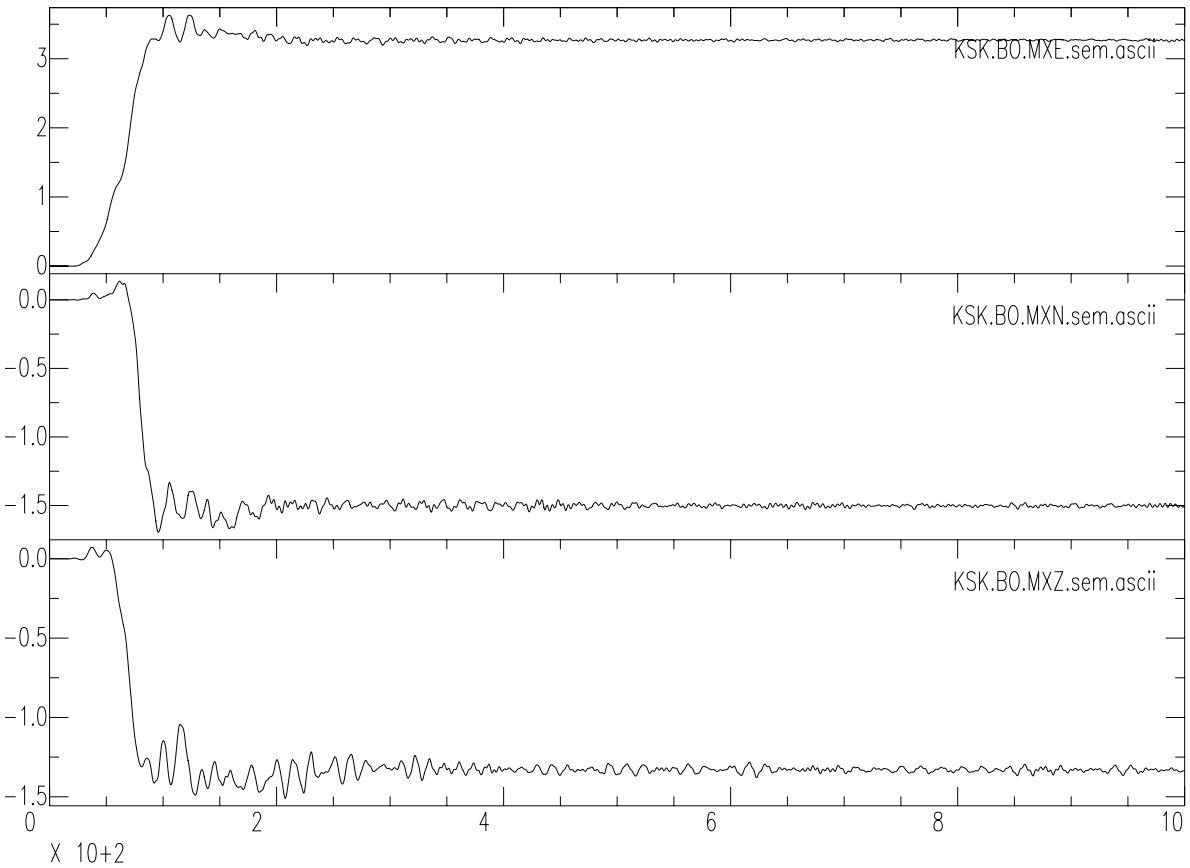

Fig. 4 Synthetic seismograms of Fnet network stations, KSK. Three component theoretical displacement seismograms are shown. 1000 sec records of EW, NS, UD are shown from top to bottom. Vertical unit is in m. Estimated static displacements are east 3.2m, south 1.5m, and down 1.3m for KSK.

(Afiamalu, Samoa Islands, epicentral distance 67 degrees), ESK (Edinburgh, U.K., 81 degrees). Each trace is bandpass filtered between 0.002 Hz and 0.1 Hz. We may say that the synthetic seismograms reproduces observed seismograms generally well for body waves. Although surface waves are not modeled well, but it is because the surface waves with this period range depend on shallow crustal structure, which may not be modeled well in the 3D mantle model. Figure 3 demonstrates example of comparison in lower frequency range for station AFI and shows that the agreement is excellent in lower frequency range. Figure 4 shows synthetics for near field station KSK (3.1 degree), of F-net broadband network in the coast of Tohoku region. Because of proximity of the station location to the epicenter, the displacement shows static displacement, whose pattern is consistent to the observed crustal deformation.

These results indicate that the synthetic seismograms computed for this finite source model reproduce observed seismograms for both near field and teleseismic stations, which suggest that this source model captures rupture properties of this earthquake.

References:

[1] Takeuchi, N., 2007. Whole mantle SH velocity model constrained by waveform inversion based on three-dimensional Born kernels, Geophys. J. Int., 169, 1153-1163.

[2] Tsuboi, S. and Takeuchi, N., 2007. Global Elastic Response Simulation, Annual Report of the Earth Simulator Center, April 2006-March 2007, 69-73.

[3] Tsuboi, S. and Takeuchi, N., 2011. Global Elastic Response Simulation, Annual Report of the Earth Simulator Center, April 2010-March 2011, 75-80.

[4] Nakamura, T., Tsuboi, S., Kaneda, Y., and Yamanaka, Y., 2010. Rupture process of the 2008 Wenchuan, China earthquake inferred from teleseismic waveform inversion and forward modeling of broadband seismic waves, Tectonophysics, 491, 72-84.

[5] Kennet, B. L. N. and Engdahl, E. R., 1991. Traveltimes for global earthquake location and phase identification. Geophys. J. Int., 105, 429.

[6] Komatitsch, D. and Tromp, J., 2002. Spectral-element simulations of global seismic wave propagation-I. Validation, Geophys. J. Int., 149, 390-412.

全地球弾性応答シミュレーション

プロジェクト責任者
坪井　誠司　　海洋研究開発機構　地球内部ダイナミクス領域 / 地球情報研究センター
著者
坪井　誠司　　海洋研究開発機構　地球内部ダイナミクス領域 / 地球情報研究センター
竹内　　希　　東京大学　地震研究所

Direct Solution 法を用いた波形インバージョンにより、地球内部マントル 3 次元地震波速度構造モデルを改善した。今回得られた新しいモデルと、これまでに得られたモデルとを比較することにより、新しいモデルでは下部マントルでの分解能が向上したことを確認した。

スペクトル要素法により現実的な 3 次元地球モデルに対する理論地震波形記録を 2011 年東北地方太平洋沖地震（Mw9.0）に対して計算した。計算は地球シミュレータの 91 ノードを用いて、周期約 5 秒の精度で行った。計算した理論地震波形は観測波形をよく説明しており、用いた地震断層モデルがよく断層における破壊過程をモデル化していることを示している。計算した地震波形は遠地観測点のみならず、近地における地殻変動のパターンも良く再現していることが分かった。

キーワード: 理論地震波形記録, 3 次元地球内部構造, スペクトル要素法